

Article

Facile Synthesis of Ni-Doped WO_{3-x} Nanosheets with Enhanced Visible-Light-Responsive Photocatalytic Performance for Lignin Depolymerization into Value-Added Biochemicals

Hao Wang^{1,2}, Yuan Li^{3,*} and Xintong Xiao^{4,*}¹ Angel Yeast Co., Ltd., Yichang 430200, China; wh21@tongji.edu.cn² College of Environmental Science and Engineering, Tongji University, Shanghai 430074, China³ School of Resource and Environmental Engineering, Wuhan Technology University, Wuhan 430200, China⁴ Central-Southern Safety and Environment Technology Institute Co., Ltd., Wuhan 430010, China

* Correspondence: liyuan83@whut.edu.cn (Y.L.); xiaoxintong2008@126.com (X.X.)

Abstract: Lignin is the only renewable resource composed of aromatic hydrocarbons in nature that can be used as raw materials for preparing chemicals. However, due to the existence of stable C–O bonds and C–C bonds in the lignin, the high-value resource utilization of lignin is still challenging work. Herein, we reported efficient lignin depolymerization using a Ni-doped WO_{3-x} nanosheet photocatalyst that was prepared via the two-step hydrothermal treatment. The optimized catalyst (Ni-doped WO_{3-x}) successfully depolymerized sodium lignosulfonate to vanillic acid and guaiacol under visible-light irradiation. The active radicals of photocatalytic depolymerization of sodium lignosulfonate were superoxide radicals, photogenic holes, and hydroxyl radicals under visible-light irradiation. Furthermore, the introduction of Ni significantly decreased the activation energy barrier for selective cleavage of the C–C bond, which was the essential step to promote lactic acid production. This work presented an effective and promising strategy for lignin depolymerization and value-added biochemical production.



Citation: Wang, H.; Li, Y.; Xiao, X. Facile Synthesis of Ni-Doped WO_{3-x} Nanosheets with Enhanced Visible-Light-Responsive Photocatalytic Performance for Lignin Depolymerization into Value-Added Biochemicals. *Catalysts* **2023**, *13*, 1205. <https://doi.org/10.3390/catal13081205>

Academic Editors: Francisco José Maldonado-Hódar, Sheng Guo, Yazi Liu and Jun Li

Received: 13 May 2023

Revised: 24 July 2023

Accepted: 7 August 2023

Published: 12 August 2023



Copyright: © 2023 by the authors. Licensee MDPI, Basel, Switzerland. This article is an open access article distributed under the terms and conditions of the Creative Commons Attribution (CC BY) license (<https://creativecommons.org/licenses/by/4.0/>).

Keywords: Ni-doped WO_{3-x} ; lignin; depolymerization; value-added biochemicals; photocatalysis

1. Introduction

Lignin is the only natural polymer that can provide a large amount of renewable aromatic groups in nature. It is rich in sources and has the potential to prepare high-value chemicals. However, due to the complexity and obstinacy of the lignin structure, most lignin is directly discharged and burned as waste, which not only pollutes the environment but also wastes resources [1,2]. As the source of aromatic structure, lignin has great potential in the preparation of aromatic compounds through depolymerization, which was the direction of lignin's future high-value utilization. Researchers have developed a variety of processes, including biocatalytic depolymerization, acid or alkali depolymerization, pyrolytic depolymerization, and catalytic depolymerization, which can convert low-value lignin into high-value products such as aromatic hydrocarbons, aldehydes, ketones, alcohols, etc. However, most of the traditional lignin catalytic depolymerization processes still require higher reaction temperatures [3–5].

Photocatalysis technology is considered a green and sustainable technology because of its advantages, such as relatively mild reaction conditions and direct use of sunlight as energy [6]. The application of photocatalysis technology to the depolymerization of lignin to obtain high-value chemicals can not only solve the problems of relatively harsh reaction conditions, resource waste, and environmental pollution encountered in traditional methods of depolymerizing lignin, but also accurately break the C–O linkage in the lignin structure to improve the yield and selectivity of value-added biochemicals [7]. The photocatalytic depolymerization of lignin uses photogenerated oxygen-containing active species

with high oxidation potential to oxidize the C–O, C–H, and C–C bonds in the substrate to obtain aromatic compounds [8]. Ugurlu et al. prepared a TiO₂-supported sepiolite catalyst via the sol-gel method, which was used for the photocatalytic depolymerization of lignin [9]. Dai et al. used MnO₂ to successfully catalyze the oxidation and further depolymerization of organic solvent lignin, sulfate lignin, and alkali lignin under blue light irradiation [10]. Wakerley et al. used a CdS/CdO_x composite photocatalyst to realize the conversion of lignocellulose to H₂ driven by solar energy [11]. Gong et al. prepared Bi and Pt loaded on TiO₂, which was used for solar-driven lignosulfonate depolymerization. The photogenic holes (h⁺) and superoxide radicals generated in the photocatalytic process convert 85% of lignosulfonate into guaiacol, vanillic acid, vanillin, 4-phenyl-1-butene-4-ol, and other intermediates [12]. Wang et al. prepared efficient TiO₂ photocatalysis materials for photocatalytic hydrogenation of lignocellulose through microstructure control and successfully obtained high-value chemicals [13]. They also used CdS quantum dots for the photocatalytic depolymerization of lignin and obtained a variety of aromatic compounds [14]. Wang et al. synthesized rod-shaped ZnIn₂S₄ photocatalytic material for the photocatalytic depolymerization of lignin into aromatic compounds [15]. The photocatalytic method was considered a green and sustainable development method due to its relatively mild reaction conditions and green and safe process. However, there were still the shortcomings of low reaction efficiency and incomplete depolymerization in the catalytic conversion of lignin using photocatalytic technology. Improving the ability of photocatalysts to activate molecular oxygen and improve the carrier separation efficiency by modifying the microstructure and band structure of photocatalysts is still a challenge, and further research is still needed.

Due to its high quantum yield, WO₃ was also widely used in the photocatalytic degradation of pollutants, photocatalytic decomposition of aquatic hydrogen, and photocatalytic reduction of CO₂ [16]. However, since the band gap of WO₃ is 2.5–3.0 eV, it can only harvest ultraviolet light in the solar spectrum. In addition, WO₃ also has a high recombination rate of photogenerated electrons and holes, resulting in a low photocatalytic efficiency of WO₃, which seriously restricts the application range of the photocatalysis of WO₃. In order to broaden the light absorption ability of WO₃ and enhance the separation ability of photogenerated electrons and holes, researchers have developed and studied many methods. Among many methods, an oxygen vacancy is considered to be a modified WO₃ technology with great advantages because it can reduce the band gap of WO_{3-x} and also prevent the recombination of photogenerated electrons and holes [17]. At present, the main methods for preparing oxygen-rich vacancy photocatalysts include metal doping, steam deposition, reduction of NaBH₄, and high-temperature calcination [12,18,19]. In these methods, transition metal doping was widely used to prepare catalysts containing oxygen vacancies because of its relatively mild reaction conditions and simple operation. It is generally believed that high-valence metals (trivalent and above) are more likely to generate oxygen vacancies because of their stronger binding force with O atoms [13]. Ti³⁺-doped TiO₂ also contains a high concentration of oxygen vacancies and thus greatly increases the photocatalytic performance of TiO₂ [20]. Yang's group fabricated a sequence of La³⁺-doped with BiOCl micro-balls that have deposited Bi nanoparticles in situ via a facile single-step solvothermal method, and excellent photocatalytic activity was obtained from not only the combined effects of La³⁺-doping but also the SPR effect of semimetal Bi [21].

At the same time, some research reports also pointed out that the doping of low-valent metals can also produce oxygen vacancies and promote the catalytic activity of photocatalysts [22–24]. However, the report on oxygen vacancies mainly considers how to generate oxygen vacancies, increase the concentration of oxygen vacancies, and improve the activity of photocatalysts [25–28]. However, the oxygen vacancy with appropriate concentration may be more important for the photocatalytic directional depolymerization of lignin into high-value chemicals. Therefore, it is of great significance to study the concentration of oxygen vacancies regulated by metals and apply them to the efficient depolymerization of lignin.

In this study, transition metal doping is used to increase the concentration of tungsten oxide oxygen vacancies, which is very beneficial to the selective depolymerization of sodium lignosulfonate as a high-value chemical. The synthesized photocatalyst showed good stability under simulated sunlight and the ability of photocatalytic degradation of sodium lignosulfonate to high-value chemicals. In addition, the mechanism of photocatalytic depolymerization of lignin was also studied in detail.

2. Results and Discussion

The phase and crystallographic structure of the synthesized samples were characterized by XRD technology, and corresponding results are shown in Figure 1a. The peaks of the above samples are well indexed to WO_3 (JCPDS No. 83-0950). The crystallinity of the 2D WO_{3-x} sample was not very good because of the ultrathin microstructure and low synthesis temperature. Hence, we could find some wide peaks in its XRD pattern. In addition, many new peaks appeared in N- WO_{3-x} because of the secondary hydrothermal treatment. However, with the increase in Ni^{2+} doping, the peak position of WO_{3-x} did not shift significantly.

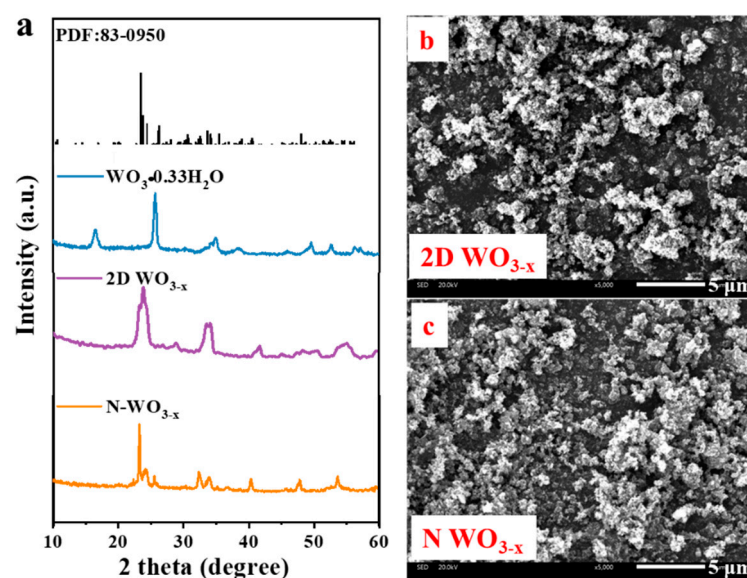


Figure 1. XRD patterns (a) and SEM images (b,c) of the prepared samples.

The microscopic morphology of the photocatalyst observed by SEM is shown in Figure 1b,c. It shows that 2D WO_{3-x} presents a diameter of about a 100 nm thin slice. With the increase in Ni^{2+} doping, WO_{3-x} thin films began to crack (Figure 1c). The reason for this phenomenon may be that the increase in Ni^{2+} inhibits the growth of some crystal planes of WO_{3-x} crystal and promotes WO_{3-x} microspheres to become ellipsoids and finally completely break into tiny flakes [26]. The TEM, HRTEM, and mapping analysis were used to obtain the microscopic morphology and structural information. As shown in Figure 2a, it is easily viewed that the N- WO_{3-x} is a regular nanosheet morphology. Additionally, all the elements are spatially distributed, as confirmed by elemental mapping (Figure 2b–e). Thus, we believe that the Ni element successfully doped WO_{3-x} nanosheets.

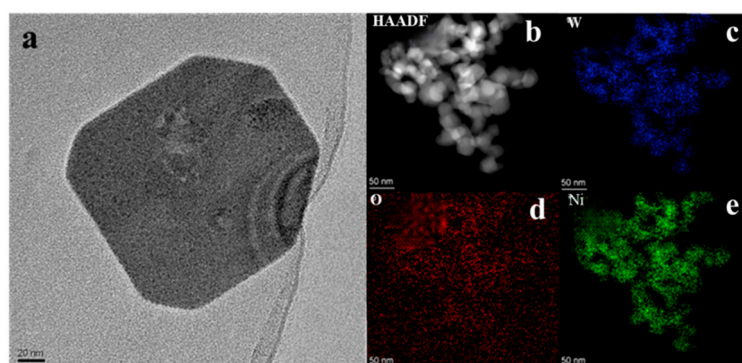


Figure 2. The TEM images (a) and the SAED image (b–e) of N-WO_{3-x}.

The surface element composition of the as-prepared samples was analyzed using XPS technology. As shown in Figure 3a, the survey spectra of samples revealed that the N-WO_{3-x} contains Ni, O, and W elements. The binding-energy (BE) peaks of W 4f were observed at 34.09 eV, 35.38 eV, 36.45 eV, and 37.47 eV (Figure 3b), which agreed with the reported BE values of the W species [28–30]. The higher energy peaks of 35.38 eV from W 4f 7/2 and 37.47 eV from W 4f 5/2 are attributed to W⁶⁺, and the lower energy peaks of 34.09 eV from W 4f 7/2 and 36.45 eV from W 4f 5/2 originated from reduced W⁵⁺ [31,32]. This result suggests that part of the W atoms were reduced to a lower valence state. As shown in Figure 3c, the binding-energy (BE) peaks of O 1s are located at 532.28, 530.77, and 530.08 eV (Figure 3c), respectively, demonstrating the peak of 532.28 eV corresponding to oxygen vacancies, the peak 530.08 eV corresponding to a bond of O–W, and the peak 530.77 eV corresponding to adsorbed oxygen, respectively [33]. To further confirm the existence of oxygen vacancies, EPR experiments were employed, which can indicate the existence of at least one unpaired electron or singly ionized oxygen vacancies. There is a significant EPR signal at $g = 2.006$ observed, which originated from the trapped electrons in the oxygen vacancies of 2D WO_{3-x} and N-WO_{3-x} (Figure 3d). It is possible that the rich oxygen vacancies can be attributed to the formation of numerous W⁵⁺ ions. Moreover, the oxygen vacancy signal of N-WO_{3-x} was significantly higher than that of 2D WO_{3-x}, indicating that Ni doping promotes the formation of oxygen vacancies in the WO_{3-x} photocatalyst [34].

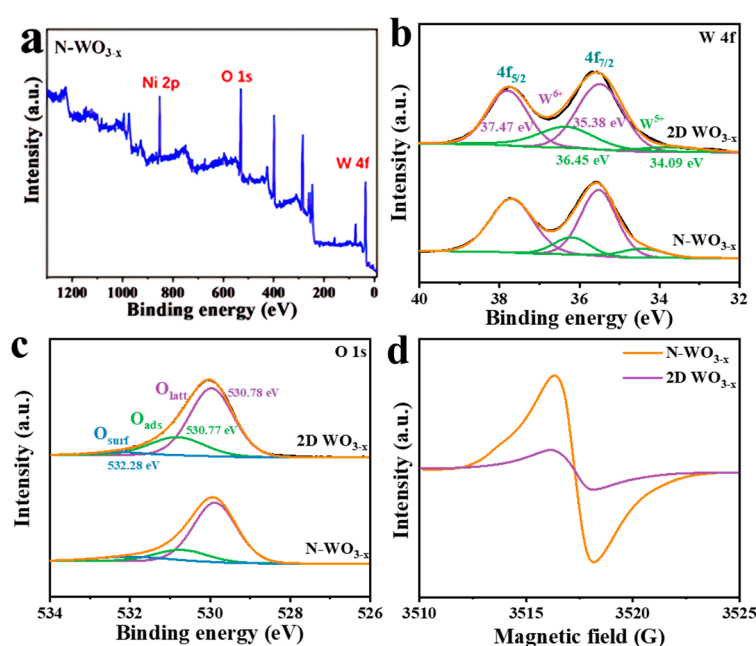


Figure 3. The XPS of Ni-doped WO_{3-x}, survey spectrum (a), XPS spectra of W4f spectra (b), XPS spectra of O 1s spectra (c), and EPR spectra (d).

The photocatalytic activity of all samples was evaluated through the experiment of photocatalytic depolymerization of sodium lignosulfonate as a high-value chemical. The results are shown in Figure 4. The depolymerization ability of the photocatalyst to sodium lignosulfonate first increases and then decreases when 3% Ni was doped into WO_{3-x} (N-WO_{3-x}), which has the best ability of photocatalytic depolymerization of sodium lignosulfonate. When the illumination time was 60 min, the depolymerization rate of sodium lignosulfonate was 80.24% (Figure 4a). In addition, compared to 2D WO_{3-x} and $\text{WO}_{3-x}\cdot 0.33\text{H}_2\text{O}$, N-WO_{3-x} also exhibited the highest catalytic activity (Figure 4b,c), which could be ascribed to how the appropriate concentration of Ni doping and oxygen vacancy can enhance the activity of the photocatalyst [35]. The scientific control in different atmosphere environments confirmed that molecular oxygen participated in the catalytic reaction and assisted in the depolymerization of lignin. Figure 5d shows that the cycling experiments also exhibit stable photocatalytic performances of N-WO_{3-x} during five cycles (Figure 4d). Thus, WO_{3-x} , with an appropriate concentration of Ni-doped and rich in oxygen vacancies, can increase the absorption capacity of light and make full use of sunlight [26,36]. The existence of oxygen vacancies can accelerate the separation of photo-generated electrons and holes, promote the formation of superoxide radicals, and improve the catalytic performance of photocatalysts.

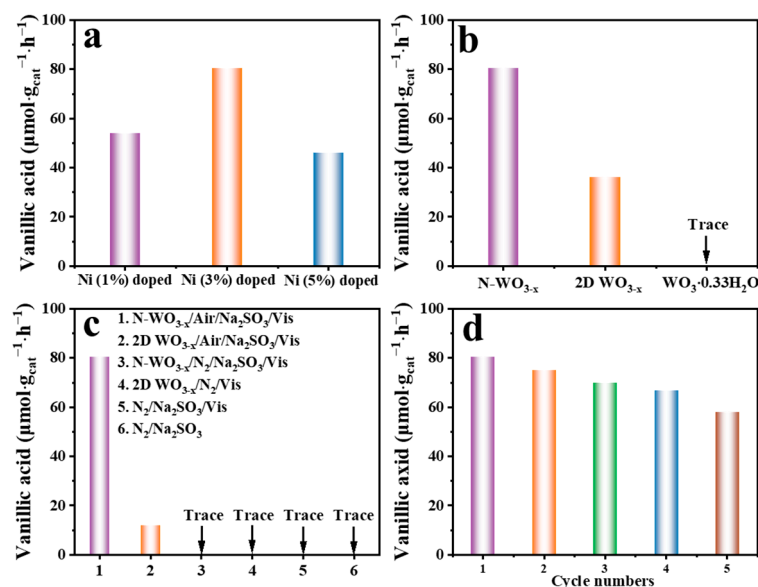


Figure 4. The photocatalytic depolymerization of sodium lignosulfonate by prepared samples with different Ni concentrations (a), the photocatalytic depolymerization of sodium lignosulfonate by different samples (b), the photocatalytic depolymerization of sodium lignosulfonate under different conditions (c), and the cyclic experiment by N-WO_{3-x} (d).

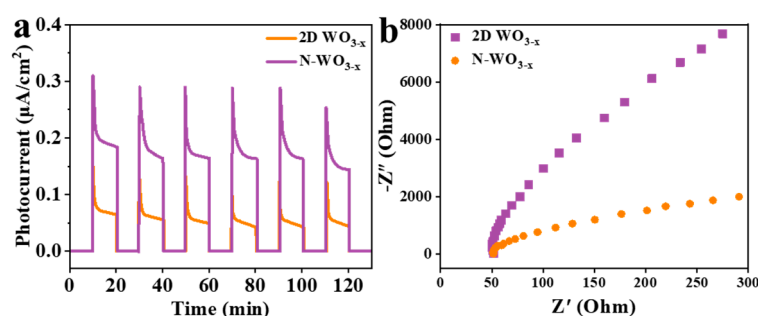


Figure 5. The transient photocurrent (a) and electrochemical impedance spectra (b) experiments of the prepared samples.

To study the separation ability of photogenerated electrons and holes of photocatalysts under simulated solar radiation, the photoelectric performance of photocatalysts was tested. Figure 5a shows the transient photocurrent curve of the synthesized sample. It shows that the synthesized photocatalysts have a certain intensity of transient photocurrent response under simulated sunlight. Among them, N-WO_{3-x} has the largest transient photocurrent response, which indicates that N-WO_{3-x} has the best photogenerated electron-hole separation ability. Additionally, to analyze the resistance of photogenerated electrons in the process of transmission, the electrochemical impedance spectra of all samples were measured. As shown in Figure 5b, compared with 2D WO_{3-x}, N-WO_{3-x} has the smallest arc radius, indicating that N-WO_{3-x} has the smallest interfacial electron transfer resistance. The transient photocurrent and the electrochemical impedance spectra proved that the N-WO_{3-x} has the optimal photogenerated electron-hole separation ability and the minimum electron transfer resistance [37].

To study the role of active radicals in the process of photocatalyst reaction, the active species were tested and analyzed by free radical capture experiment. The results are shown in Figure 6a. It showed that when p-benzoquinone, triethanolamine, and tert-butanol were added to the reaction system, the degradation rate of sodium lignosulfonate decreased to a certain extent. Among them, the degradation rate of sodium lignosulfonate decreased most significantly after the addition of tert-butyl alcohol, indicating that the photocatalytic reaction system was a free radical reaction mechanism with the hydroxyl radical as the main component and the photogenic hole and superoxide radical as the auxiliary component. The optical absorption performance of the synthesized sample was analyzed by a UV-Vis diffuse reflectance spectrometer, and the results are shown in Figure 6b. It shows that all photocatalysts have the ability to absorb ultraviolet light. Compared with 2D WO_{3-x}, N-WO_{3-x} shows a slight redshift and a significant tailing phenomenon at the wavelength of 400 nm, which may be caused by Ni doping and the formation of oxygen vacancies [26,34,35]. On the other hand, as shown in Figure 6c, comparing to the binding energy of 2D WO_{3-x}, that of at about 0 eV was attributed to the doped Ni²⁺, which changed the electronic structure of the sample [36–39], which also proves that the Ni element was doped into the lattice of WO_{3-x}. The valence bands of the N-WO_{3-x} and 2D WO_{3-x} were 1.97 and 1.82 eV, respectively. Thus, the conduction band potentials of the N-WO_{3-x} and 2D WO_{3-x} were calculated to be −0.20 and −0.57 eV, respectively, according to the formula $E_g = E_{VB} - E_{CB}$. The band structure of the N-WO_{3-x} and 2D WO_{3-x} is clearly depicted in Figure 6d. Obviously, the conduction band edge of N-WO_{3-x} moved in a more negative direction, which promoted the combination of N-WO_{3-x} and O₂ to form superoxide radicals, which is consistent with the results of the free radical capture experiment.

Based on the above discussion and previous research results [38], a possible mechanism of the photocatalytic depolymerization of sodium lignosulfonate with N-WO_{3-x} was proposed. When the simulated sunlight irradiates the N-WO_{3-x} photocatalyst, the photogenerated electrons in the valence band of N-WO_{3-x} are rapidly excited and transferred to the conduction band. For pure WO_{3-x}, more photogenerated electrons will recombine with holes again, reducing the photocatalytic efficiency. However, the N-WO_{3-x} photocatalyst contains numerous oxygen vacancies, which can trap O₂ and react with the photogenerated electrons transferred to the conduction band, forming superoxide radicals. Because of its mild oxidation potential, superoxide can rapidly oxidize organic intermediates into high-value chemicals without oxidizing and decomposing intermediate products to form CO₂ and H₂O [40]. After being consumed by O₂, the photogenerated electrons leave behind holes in the valence band. Then, the partial photogenerated holes would oxidize water to generate hydroxyl radicals, while the other photogenerated holes would directly oxidize sodium lignosulfonate into the organic intermediates CO₂ and H₂O. Meanwhile, the hydroxyl radical with a high oxidation potential can oxidize sodium lignosulfonate and small molecular organic intermediates to form small molecular organic intermediates, CO₂ and H₂O, further reducing the yield of organic compounds in the photocatalytic reaction [40].

This is also the reason why the yields of vanillic acid and vanillin first increased and then decreased in the photocatalytic degradation of sodium lignosulfonate.

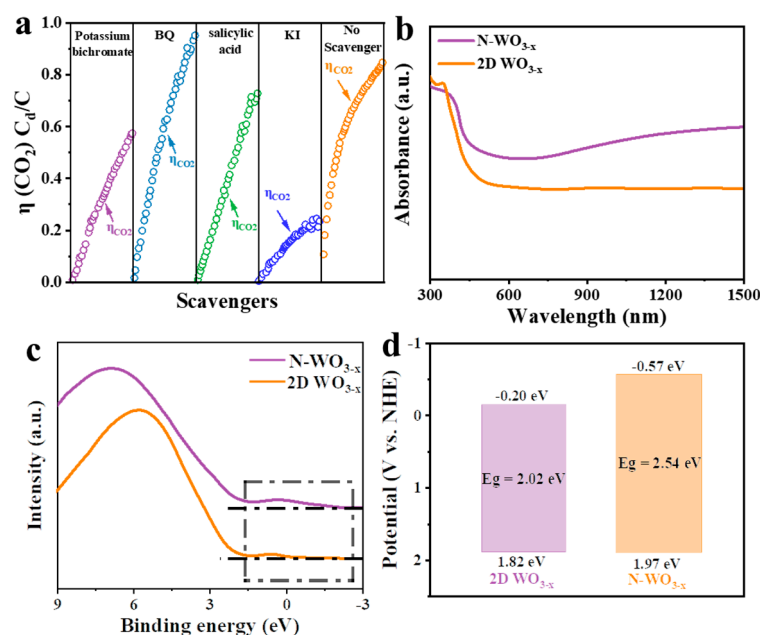


Figure 6. Free radical capture experiment (a), DRS (b), binding energy (c), and potential band structures (d) of the prepared samples.

The appropriate concentration of Ni doping and the formation of the appropriate concentration of oxygen vacancies can promote the production of superoxide radicals to a certain extent. According to previous research, superoxide radicals exhibit mild oxidation potential [41,42], which is beneficial to the stability of depolymerization products. At the same time, superoxide radicals can also facilitate the separation of photogenerated electrons and holes. However, increasing the concentration of oxygen vacancies inevitably leads to the formation of hydroxyl radicals and photogenerated holes, causing the degradation of sodium lignosulfonate in the reaction system into H_2O and CO_2 , thereby reducing the yield of high-value chemicals. Therefore, it is crucial to form the appropriate concentration of oxygen vacancies through Ni-doping to increase the yield of high-value chemicals in the photocatalytic depolymerization process of sodium lignosulfonate.

3. Materials and Methods

3.1. Materials and Reagents

All analytical grade reagents were purchased from Sinopharm Chemical Reagent Co. Ltd. (Shanghai, China). and used directly without further purification. Sodium lignosulfonate was from Angel Yeast Co. Ltd. (Yichang, China).

3.2. Preparation of Photocatalysts

The detailed steps of synthesis process of Ni^{2+} doped WO_{3-x} rich in oxygen vacancies were as follows.

Firstly, the WO_{3-x} nanosheets were synthesized through a precursor solvothermal method. In brief, 0.5 g of sodium tungstate was initially dissolved into 150 mL of deionized water (80 °C). Then, 150 mL of nitric acid was slowly dropped into the tungstate solution while stirred for 30 h to obtain a bright yellow suspension. Subsequently, the bright yellow precursor, $\text{WO}_3 \cdot 0.33\text{H}_2\text{O}$, was obtained by centrifuging and drying at 60 °C in an oven. Herein, 0.25 g of the ground $\text{WO}_3 \cdot 0.33\text{H}_2\text{O}$ was poured into 50 mL methanol while vigorously stirred for 30 min to obtain mixed suspension. Then, 15 mL of acetic acid was dropped into the yellow suspension while stirred for another 15 min. Then, the above

suspension was transferred into a 90 mL PPL-lined stainless-steel autoclave and heated at 220 °C for 30 h in an oven. After naturally cooling to room temperature, the blue sample was centrifuged and washed with water and ethanol, respectively. Finally, the prepared nanosheets were heated at 550 °C for 2 h at a 10% H₂: 90% Ar atmosphere. The pure WO_{3-x} nanosheets were named 2D WO_{3-x}.

Secondly, 5 mL of ethylene glycol and 75 mL of anhydrous ethanol were added to a 100 mL beaker, respectively, and stirred continuously for 30 min and labeled as A. Next, 0.830 g of prepared WO_{3-x} nanosheets and 0~0.06 g (0~5% of total mass) of nickel nitrate hexahydrate were added to solution A and stirred continuously for 30 min. Subsequently, the above solution was transferred to PPL-lined stainless-steel autoclave for hydrothermal reaction. The reaction temperature was 160 °C, and the reaction time was 12 h. After the reaction, the stainless-steel reactor was naturally cooled to room temperature, and then the obtained light-yellow product was centrifugally washed with water and ethanol three times. After that, the product was dried in a vacuum-drying oven at 60 °C overnight to obtain a Ni²⁺ doped WO_{3-x} photocatalyst rich in oxygen vacancies. The sample with the best doping ratio (3%) was named N-WO_{3-x}.

3.3. Characterization

The structure and crystallinity of the prepared samples were characterized by X-ray diffraction (XRD, D/MAX-RB, Rigaku, Tokyo, Japan) analysis on a D/MAX-RB diffractometer with Cu K α radiation under the operation conditions of 40 kV and 50 mA. Transmission electron microscopy (TEM, JEM-2100F, JEOL, Tokyo, Japan), high-resolution transmission electron microscopy (HRTEM), and selected area electron diffraction (SAED, JEM2100F, 280 kV) were used to characterize the morphology and microstructure of the prepared samples. X-ray photoelectron spectroscopy (XPS, ESCALAB Xi, Thermo Fisher, Scientific Co., Ltd., Waltham, MA, USA) was employed to analyze the valence states of the elements with a monochromatic Mg K α source and a charge neutralizer. The binding energies obtained in the XPS spectral analysis were adjusted for specimen charging by referencing C 1s at 284.5 eV. The transmittance for each composite film was measured on a Lambda 750 S UV/Vis/NIR Spectrometer (DRS, Lambda 750 S, PerkinElmer, Waltham, MA, USA). Photoluminescence (PL) emission spectra were collected by an RF-5301PC spectrofluorometer (Shimadzu, Japan) with an emission wavelength of 312 nm. The ESR experiments were recorded by an electron paramagnetic resonance (EPR, A300-10, Bruker, Billerica, MA, USA) spectrometer () to detect the unpaired electron or singly ionized oxygen vacancies.

3.4. Photocatalytic Activity Test

The activity of the photocatalyst was evaluated by studying the depolymerization ability of the photocatalyst to sodium lignosulfonate, and the light source was treated with a 400 nm cut-off filter. The experimental steps of photocatalytic activity evaluation were as follows. First, 50 mL of 0.1 g/L sodium lignosulfonate was added to the photocatalytic reactor with a volume of 100 mL. Then, 0.01 g of photocatalyst was added to the solution, and it was left in the shade for 1 h to achieve adsorption–desorption equilibrium. After dark adsorption, the light source was turned on. Every 20 min, 3 mL of liquid was carefully extracted with a 5 mL syringe, and a 0.22 μ m nylon filtration membrane was used for filtration. The concentration of sodium lignosulfonate in the filtered liquid was analyzed and calculated by UV-Vis spectrophotometer. The characteristic adsorption wavelength of sodium lignosulfonate was 280 nm. Additionally, to analyze the content of high-value chemicals obtained after the depolymerization of sodium lignosulfonate, the liquid was filtered after the photocatalytic reaction, extracted with dichloromethane three times, and then evaporated to remove dichloromethane. After that, the organic matter was redissolved with chromatography-grade acetonitrile and analyzed by HPLC. The test conditions were as follows. The separation column was the C-18 column produced by Shimadzu Company, the mobile phase was acetonitrile and water, the volume ratio was 6:4, the flow rate of the mobile phase was 0.6 mL/min, and the test wavelength was 280 nm. Finally, to study

the mechanism of active radicals in the depolymerization of sodium lignosulfonate by photocatalyst, the tert-butyl alcohol (4 mM), triethanolamine (4 mM), silver nitrate (4 mM), and 1,4-p-benzoquinone (2 mM) were respectively added to the photocatalytic reaction system to carry out the experiment of photocatalytic depolymerization of lignin, and the experimental steps of photocatalytic depolymerization of sodium lignosulfonate.

4. Conclusions

In this study, Ni-doped WO_{3-x} nanosheets with appropriate concentrations of oxygen vacancy were successfully synthesized by the solvothermal method. The doping of Ni reduced the band gap of the WO_{3-x} photocatalyst, increasing its absorption ability to UV-visible light. Additionally, doped Ni also increased the concentration of oxygen vacancies, promoting the separation efficiency of photogenerated electrons and holes to some extent and enhancing the catalytic performance of the photocatalysts. The Ni-doped WO_{3-x} photocatalyst can successfully depolymerize sodium lignosulfonate to vanillic acid, vanillin, guaiacol, CO_2 , and H_2O . The active radicals of photocatalytic depolymerization of sodium lignosulfonate are superoxide radicals, photogenic holes, and hydroxyl radicals. Because the higher concentration of oxygen vacancies increases the concentration of superoxide radicals in the photocatalysis system, it also increases the concentration of hydroxyl radicals and photogenerated holes, resulting in the photocatalyst decomposing more sodium lignosulfonate or depolymerized products into CO_2 and H_2O , reducing the yield of high-value chemicals. Therefore, suitable Ni doping and oxygen vacancy concentration were very necessary to promote the conversion of sodium lignosulfonate into high-value chemicals through photocatalytic depolymerization. This study provides a new idea for controlling the oxygen vacancy concentration in WO_{3-x} through doping and promoting the photocatalytic depolymerization of sodium lignosulfonate as high-value chemicals.

Author Contributions: Conceptualization, Y.L.; funding acquisition, H.W.; formal analysis, H.W.; project administration, Y.L.; supervision, Y.L.; writing—original draft preparation, H.W.; rewriting and re-editing, X.X. All authors have read and agreed to the published version of the manuscript.

Funding: This work received financial support from the Angel Yeast Co. Ltd (Y02F013522006).

Data Availability Statement: The data presented in this study are openly available.

Conflicts of Interest: The authors declare no conflict of interest.

References

1. Puscaselu, R.G.; Lobiuc, A.; Dimian, M.; Covasa, M. Alginate: From food industry to biomedical applications and management of metabolic disorders. *Polymers* **2020**, *12*, 10.
2. Seddiqi, H.; Oliaei, E.; Honarkar, H.; Jin, J.F.; Geonzon, L.C.; Bacabac, R.G.; Klein-Nulend, J. Cellulose and its derivatives: Towards biomedical applications. *Cellulose* **2021**, *28*, 1893–1931. [[CrossRef](#)]
3. Anitha, A.; Sowmya, S.; Kumar, P.T.S.; Deepthi, S.; Chennazhi, K.P.; Ehrlich, H.; Tsurkan, M.; Jayakumar, R. Chitin and chitosan in selected biomedical applications. *Prog. Polym. Sci.* **2014**, *39*, 1644–1667. [[CrossRef](#)]
4. Zhang, J.F.; Jiang, Y.; Easterling, L.F.; Anstner, A.; Li, W.R.; Alzarini, K.Z.; Dong, X.M.; Bozell, J.; Kenttämaa, H.I. Compositional analysis of organosolv poplar lignin by using high-performance liquid chromatography/high-resolution multi-stage tandem mass spectrometry. *Green Chem.* **2021**, *23*, 983–1000. [[CrossRef](#)]
5. Cheng, G.; Zhang, X.; Simmons, B.; Singh, S. Theory, practice and prospects of X-ray and neutron scattering for lignocellulosic biomass characterization: Towards understanding biomass pretreatment. *Energy. Environ. Sci.* **2015**, *8*, 436–455. [[CrossRef](#)]
6. Hill, C.; Modification, W. *Chemical, Thermal, and Other Processes*; John Wiley & Sons: Chichester, UK, 2006.
7. Sun, Z.H.; Fridrich, B.; de Santi, A.; Elangovan, S.; Barta, K. Bright side of lignin depolymerization: Toward new platform chemicals. *Chem. Rev.* **2018**, *118*, 614–678. [[CrossRef](#)] [[PubMed](#)]
8. Wang, M.; Liu, M.; Lu, J.; Wang, F. Photo splitting of bio-polyols and sugars to methanol and syngas. *Nat. Commun.* **2020**, *11*, 1083. [[CrossRef](#)]
9. Ugurlu, M.; Karaoglu, M.H. TiO_2 supported on sepiolite: Preparation, structural and thermal characterization and catalytic behavior in photocatalytic treatment of phenol and lignin from olive mill wastewater. *Chem. Eng. J.* **2011**, *166*, 859–867. [[CrossRef](#)]
10. Dai, J.; Patti, A.F.; Styles, G.N.; Nanayakkara, S.; Spiccia, L.; Arena, F.; Italiano, C.; Saito, K. Lignin oxidation by MnO_2 under the irradiation of blue light. *Green Chem.* **2019**, *21*, 2005–2014. [[CrossRef](#)]

11. Wakerley, D.W.; Kuehnel, M.F.; Orchard, K.L.; Ly, K.H.; Rosser, T.E.; Reisner, E. Solar-driven reforming of lignocellulose to H₂ with a CdS/CdOx photocatalyst. *Nat. Energy* **2017**, *2*, 17021–17028. [[CrossRef](#)]
12. Gong, J.; Imbault, A.; Farnood, R. The promoting role of bismuth for the enhanced photocatalytic oxidation of lignin on Pt-TiO₂ under solar light illumination. *Appl. Catal. B* **2017**, *204*, 296–303. [[CrossRef](#)]
13. Wu, X.J.; Li, J.Q.; Xie, S.J.; Duan, P.; Zhang, H.; Feng, J.; Zhang, Q.; Cheng, J.; Wang, Y. Selectivity control in photocatalytic valorization of biomass-derived platform compounds by surface engineering of titanium oxide. *Chem* **2020**, *6*, 3038–3053. [[CrossRef](#)]
14. Wu, X.J.; Fan, X.T.; Xie, S.J.; Lin, J.; Cheng, J.; Zhang, Q.; Chen, L.; Wang, Y. Solar energy-driven lignin-first approach to full utilization of lignocellulosic biomass under mild conditions. *Nat. Catal.* **2018**, *1*, 772–780. [[CrossRef](#)]
15. Luo, N.C.; Wang, M.; Li, H.J.; Zhang, J.; Hou, T.; Chen, H.; Zhang, X.; Lu, J.; Wang, F. Visible-light-driven self-hydrogen transfer hydrogenolysis of lignin models and extracts into phenolic products. *ACS Catal.* **2017**, *7*, 4571–4580. [[CrossRef](#)]
16. Shandilya, P.; Sambyal, S.; Sharma, R.; Mandyal, P.; Fang, B.Z. Properties, optimized morphologies, and advanced strategies for photocatalytic applications of WO₃ based photocatalysts. *J. Hazard. Mater.* **2022**, *428*, 128218. [[CrossRef](#)]
17. Ma, M.; Zhang, K.; Li, P.; Jung, S.M.; Jeong, J.M.; Park, H.J. Dual oxygen and tungsten vacancies on a WO₃ photoanode for enhanced water oxidation. *Angew. Chem. Int. Edit.* **2016**, *55*, 11819–11823. [[CrossRef](#)]
18. Lu, Y.F.; Huang, Y.; Zhang, Y.F.; Huang, T.T.; Li, H.W.; Cao, J.J.; Ho, W.K. Effects of H₂O₂ generation over visible light-responsive Bi/Bi₂O_{2-x}CO₃ nanosheets on their photocatalytic NOx removal performance. *Chem. Eng. J.* **2019**, *363*, 374–382. [[CrossRef](#)]
19. Li, H.; Qin, F.; Yang, Z.P.; Cui, X.M.; Wang, J.F.; Zhang, L.Z. New reaction pathway induced by plasmon for selective benzyl alcohol oxidation on BiOCl possessing oxygen vacancies. *J. Am. Chem. Soc.* **2017**, *139*, 3513–3521. [[CrossRef](#)]
20. Peng, H.P.; Yang, T.; Lin, H.P.; Xu, Y.; Wang, Z.H.; Zhang, Q.H.; Liu, S.H.; Geng, H.B.; Gu, L.; Wang, C.; et al. Ru/In dual-single atoms modulated charge separation for significantly accelerated photocatalytic H₂ evolution in pure water. *Adv. Energy. Mater.* **2022**, *12*, 2201688. [[CrossRef](#)]
21. Yang, J.; Liang, Y.J.; Li, K.; Yang, G.; Zhu, Y.L.; Liu, S.Q.; Lei, W. New reaction pathway induced by the synergistic effects of Bi plasmon and La³⁺ doping for efficient visible light photocatalytic reaction on BiOCl. *Appl. Surf. Sci.* **2018**, *58*, 769–780. [[CrossRef](#)]
22. Kim, Y.H.; Kim, S.Y.; Kim, K.J.; Kim, C.Y.; Jang, J.H.; Kim, Y.M.; Lee, H. Multiscale probing of the influence of the defect induced variation of oxygen vacancies on the photocatalytic activity of doped ZnO nanoparticle. *J. Mater. Chem. A* **2020**, *8*, 25345–25354. [[CrossRef](#)]
23. Zhang, N.; Li, L.G.; Wang, J.; Hu, Z.W.; Shao, Q.; Xiao, X.H.; Huang, X.Q. Surface-regulated rhodium–antimony nanorods for nitrogen fixation. *Angew. Chem. Int. Ed.* **2020**, *59*, 8066–8071. [[CrossRef](#)]
24. Zhao, Y.X.; Zhao, Y.F.; Shi, R.; Wang, B.; Waterhouse, G.I.N.; Wu, L.Z.; Tung, C.H.; Zhang, T.R. Tuning oxygen vacancies in ultrathin TiO₂ nanosheets to boost photocatalytic nitrogen fixation up to 700 nm. *Adv. Mater.* **2019**, *31*, 1806482. [[CrossRef](#)]
25. Cheng, Q.; Yang, Z.X.; Li, Y.; Wang, J.T.; Wang, J.Q.; Zhang, G.K. Amorphous/crystalline Cu_{1.5}Mn_{1.5}O₄ with rich oxygen vacancies for efficiently photothermocatalytic mineralization of toluene. *Chem. Eng. J.* **2023**, *471*, 144295. [[CrossRef](#)]
26. Xu, J.; Li, M.; Yang, L.Y.; Qiu, J.H.; Chen, Q.; Zhang, X.F.; Feng, Y.; Yao, J.F. Synergy of Ni dopant and oxygen vacancies in ZnO for efficient photocatalytic depolymerization of sodium lignosulfonate. *Chem. Eng. J.* **2020**, *394*, 125050. [[CrossRef](#)]
27. Lu, C.H.; Li, X.R.; Wu, Q.; Li, J.; Wen, L.; Dai, Y.; Huang, B.B.; Li, B.J.; Lou, Z.Z. Constructing surface plasmon resonance on Bi₂WO₆ to boost high-selective CO₂ reduction for methane. *ACS Nano* **2021**, *15*, 3529–3539. [[CrossRef](#)] [[PubMed](#)]
28. Yang, Z.X.; Wang, J.Q.; Wang, J.T.; Li, M.; Cheng, Q.; Wang, Z.Z.; Wang, X.T.; Li, J.M.; Li, Y.; Zhang, G.K. 2D WO_{3-x} Nanosheet with rich oxygen vacancies for efficient visible-light-driven photocatalytic nitrogen fixation. *Langmuir* **2022**, *3*, 1178–1187. [[CrossRef](#)]
29. Li, Y.; Li, J.; Zhang, G.K.; Wang, K.; Wu, X.Y. Selective photocatalytic oxidation of low concentration methane over graphitic carbon nitride-decorated tungsten bronze cesium. *ACS Sustain. Chem. Eng.* **2019**, *7*, 4382–4389. [[CrossRef](#)]
30. Bai, S.; Jiang, J.; Zhang, Q.; Xiong, Y.J. Steering charge kinetics in photocatalysis: Intersection of materials syntheses, characterization techniques and theoretical simulations. *Chem. Soc. Rev.* **2015**, *44*, 2893. [[CrossRef](#)]
31. Shi, R.; Zhao, Y.X.; Waterhouse, G.I.N.; Zhang, S.; Zhang, T.R. Defect engineering in photocatalytic nitrogen fixation. *ACS Catal.* **2019**, *9*, 9739–9750. [[CrossRef](#)]
32. Wang, D.; Li, Y.; Wen, L.S.; Xi, J.B. Ni-Pd incorporated Fe₃O₄ yolk-shelled nanospheres as efficient magnetically recyclable catalysts for reduction of N-containing unsaturated compounds. *Catalysts* **2023**, *13*, 190. [[CrossRef](#)]
33. Liang, C.; Niu, H.Y.; Guo, H.; Niu, C.G.; Huang, D.W.; Yan, Y.Y.; Liu, H.Y.; Shao, B.B.; Feng, H.P. Insight into photocatalytic nitrogen fixation on graphitic carbon nitride: Defect-dopant strategy of nitrogen defect and boron dopant. *Chem. Eng. J.* **2020**, *396*, 125395. [[CrossRef](#)]
34. Huang, B.J.; Fu, X.X.; Wang, K.; Wang, L.; Zhang, H.L.; Liu, Z.Y.; Liu, B.; Li, J. Chemically bonded BiVO₄/Bi₁₉Cl₃S₂₇ heterojunction with fast hole extraction dynamics for continuous CO₂ photoreduction. *Adv. Powder Mater.* **2023**, 100140. [[CrossRef](#)]
35. Wang, H.Y.; Niu, R.R.; Liu, J.H.; Guo, S.; Yang, Y.P.; Liu, Z.Y.; Li, J. Electrostatic self-assembly of 2D/2D CoWO₄/g-C₃N₄ p-n heterojunction for improved photocatalytic hydrogen evolution: Built-in electric field modulated charge separation and mechanism unveiling. *Nano Res.* **2022**, *15*, 6987–6998. [[CrossRef](#)]
36. Chen, X.; Zhang, X.; Li, Y.H.; Qi, M.Y.; Li, J.Y.; Tang, Z.R.; Zhou, Z.; Xu, Y.J. Transition metal doping BiOBr nanosheets with oxygen vacancy and exposed {102} facets for visible light nitrogen fixation. *Chem. Eng. J.* **2021**, *281*, 119516. [[CrossRef](#)]
37. Wang, S.Y.; Hai, X.; Ding, X.; Chang, K.; Xiang, Y.G.; Meng, X.G.; Yang, Z.X.; Chen, H.; Ye, J.H. Light-switchable oxygen vacancies in ultrafine Bi₅O₇Br nanotubes for boosting solar-driven nitrogen fixation in pure water. *Adv. Mater.* **2017**, *29*, 1701774. [[CrossRef](#)]

38. Li, C.C.; Wang, T.; Zhao, Z.J.; Yang, W.M.; Li, J.F.; Li, A.; Yang, Z.L.; Ozin, G.A.; Gong, J.L. Promoted fixation of molecular nitrogen with surface oxygen vacancies on plasmon-enhanced TiO₂ photoelectrodes. *Angew. Chem. Int. Ed.* **2018**, *57*, 5278–5282. [[CrossRef](#)]
39. Liu, Q.Y.; Wang, H.D.; Tang, R.; Cheng, Q.; Yuan, Y.J. Rutile TiO₂ nanoparticles with oxygen vacancy for photocatalytic nitrogen fixation. *ACS Appl. Nano Mater.* **2021**, *4*, 8674–8679. [[CrossRef](#)]
40. Li, J.; Wu, X.Y.; Pan, W.F.; Zhang, G.K.; Chen, H. Vacancy-rich monolayer BiO_{2-x} as highly efficient UV, visible and near-infrared responsive photocatalyst. *Angew. Chem. Int. Ed.* **2018**, *57*, 491–495. [[CrossRef](#)] [[PubMed](#)]
41. Wu, X.; Zhang, W.; Li, J.; Xiang, Q.J.; Liu, Z.Y.; Liu, B. Identification of the active sites on metallic MoO_{2-x} nano-sea-urchin for atmospheric CO₂ photoreduction under UV, visible, and near-infrared light illumination. *Angew. Chem. Int. Ed.* **2023**, *62*, e202213124. [[CrossRef](#)]
42. Niu, R.R.; Liu, Q.Y.; Huang, B.J.; Liu, Z.Y.; Zhang, W.F.; Peng, Z.K.; Wang, Z.Y.; Yang, Y.P.; Gu, Z.K.; Li, J. Black phosphorus/Bi₁₉Br₃S₂₇ van der Waals heterojunctions ensure the supply of activated hydrogen for effective CO₂ photoreduction. *Appl. Catal. B* **2022**, *317*, 121727. [[CrossRef](#)]

Disclaimer/Publisher's Note: The statements, opinions and data contained in all publications are solely those of the individual author(s) and contributor(s) and not of MDPI and/or the editor(s). MDPI and/or the editor(s) disclaim responsibility for any injury to people or property resulting from any ideas, methods, instructions or products referred to in the content.